

Dynamic full-field optical coherence tomography allows live imaging of retinal pigment epithelium stress model

Kassandra Groux, Anna Verschueren, Céline Nanteau, Marilou Clémençon, Mathias Fink, José-Alain Sahel, Claude Boccara, Michel Paques, Sacha Reichman, Kate Grieve

▶ **To cite this version:**

Kassandra Groux, Anna Verschueren, Céline Nanteau, Marilou Clémençon, Mathias Fink, et al.. Dynamic full-field optical coherence tomography allows live imaging of retinal pigment epithelium stress model. Communications Biology, 2022, 5 (1), pp.575. 10.1038/s42003-022-03479-6 . inserm-03726483

HAL Id: inserm-03726483
https://inserm.hal.science/inserm-03726483

Submitted on 18 Jul 2022

HAL is a multi-disciplinary open access archive for the deposit and dissemination of scientific research documents, whether they are published or not. The documents may come from teaching and research institutions in France or abroad, or from public or private research centers.

L'archive ouverte pluridisciplinaire **HAL**, est destinée au dépôt et à la diffusion de documents scientifiques de niveau recherche, publiés ou non, émanant des établissements d'enseignement et de recherche français ou étrangers, des laboratoires publics ou privés.

communications biology

ARTICLE

https://doi.org/10.1038/s42003-022-03479-6 OPEN

Dynamic full-field optical coherence tomography allows live imaging of retinal pigment epithelium stress model

Kassandra Groux[1,2✉], Anna Verschueren[2,3], Céline Nanteau[3], Marilou Clémençon[3], Mathias Fink[1], José-Alain Sahel[2,3,4,5], Claude Boccara[1], Michel Paques[2], Sacha Reichman[3] & Kate Grieve[2,3✉]

Retinal degenerative diseases lead to the blindness of millions of people around the world. In case of age-related macular degeneration (AMD), the atrophy of retinal pigment epithelium (RPE) precedes neural dystrophy. But as crucial as understanding both healthy and pathological RPE cell physiology is for those diseases, no current technique allows subcellular in vivo or in vitro live observation of this critical cell layer. To fill this gap, we propose dynamic full-field OCT (D-FFOCT) as a candidate for live observation of in vitro RPE phenotype. In this way, we monitored primary porcine and human stem cell-derived RPE cells in stress model conditions by performing scratch assays. In this study, we quantified wound healing parameters on the stressed RPE, and observed different cell phenotypes, displayed by the D-FFOCT signal. In order to decipher the subcellular contributions to these dynamic profiles, we performed immunohistochemistry to identify which organelles generate the signal and found mitochondria to be the main contributor to D-FFOCT contrast. Altogether, D-FFOCT appears to be an innovative method to follow degenerative disease evolution and could be an appreciated method in the future for live patient diagnostics and to direct treatment choice.

[1] Institut Langevin, ESPCI Paris-PSL, CNRS, 10 rue Vauquelin, Paris 75005, France. [2] Paris Eye Imaging Group, Quinze-Vingts National Eye Hospital, INSERM-DGOS, CIC 1423, 28 rue de Charenton, Paris 75012, France. [3] Institut de la Vision, Sorbonne Université, INSERM, CNRS, 17 rue Moreau, Paris F-75012, France. [4] Department of Ophthalmology, Fondation Ophtalmologique Adolphe de Rotschild, F-75019 Paris, France. [5] Department of Ophthalmology, The University of Pittsburgh School of Medicine, Pittsburgh, PA 15213, USA. ✉email: kassandra.groux@gmail.com; kategrieve@gmail.com

The retinal pigment epithelium (RPE) is the most external layer of the retina, placed between the photoreceptors which collect the light and the blood supply from the choroid[1]. RPE is a cell monolayer composed of hexagonal cells with a basal nucleus, containing a variety of organelles. On the basal surface, the RPE is linked to the choroidal vasculature, while on the apical surface, RPE cells have microvilli which grab the photoreceptor outer segments to maintain the integrity of the retina[2]. The RPE layer is affected in degenerative diseases, such as age-related macular degeneration (AMD)[3–5]. AMD is one of the leading causes of blindness in developed countries, affecting 170 million people worldwide[6]. In late form dry AMD, called geographic atrophy, it may lead to expanding atrophic foci of the RPE. Little is known about the mechanisms underlying the propagation of RPE atrophy. Animal models were used to model AMD. However, the environmental conditions are less controllable than for a cell-based model, such as RPE cells[7], used to test drug therapies or the involvement of proteins in AMD. By following the behaviour of RPE in culture in response to damage, we take a step towards mimicking formation of geographic atrophy lesions in AMD. Future developments will use multi-layered cell-based models, including other layers of the retina or the choroid to match in vivo conditions.

Dynamic Full-Field OCT (D-FFOCT) has recently been presented as a non-invasive live imaging technique suitable for the study of 2D and 3D cell cultures[8,9]. Intracellular organelle movement is known to generate the D-FFOCT signal, but the precise identity of the organelles has not yet been deciphered. RPE cells have also been imaged with electron microscopy[10], but this technique does not allow live-cell imaging, preventing the imaging of organelle dynamics. Live-cell imaging is possible with several imaging techniques, but certain requirements have to be met. It is important to keep the cell cultures healthy to image them over long periods of time, meaning avoiding photo-toxicity. Imaging methods such as fluorescence imaging techniques, multiphoton microscopy, or widefield systems, have been applied to live-cell imaging[11]. However, many of these techniques require the use of invasive fluorophores, preventing continued use of the sample after the imaging. Others, such as widefield systems, usually have a low lateral resolution and do not have optical sectioning for 3D imaging. The use of spinning-disc confocal microscopy for RPE live-cell imaging has been demonstrated[12,13], but shows significant problems with autofluorescence background in images and the impossibility to reuse the samples after the imaging due again to the use of invasive fluorophores.

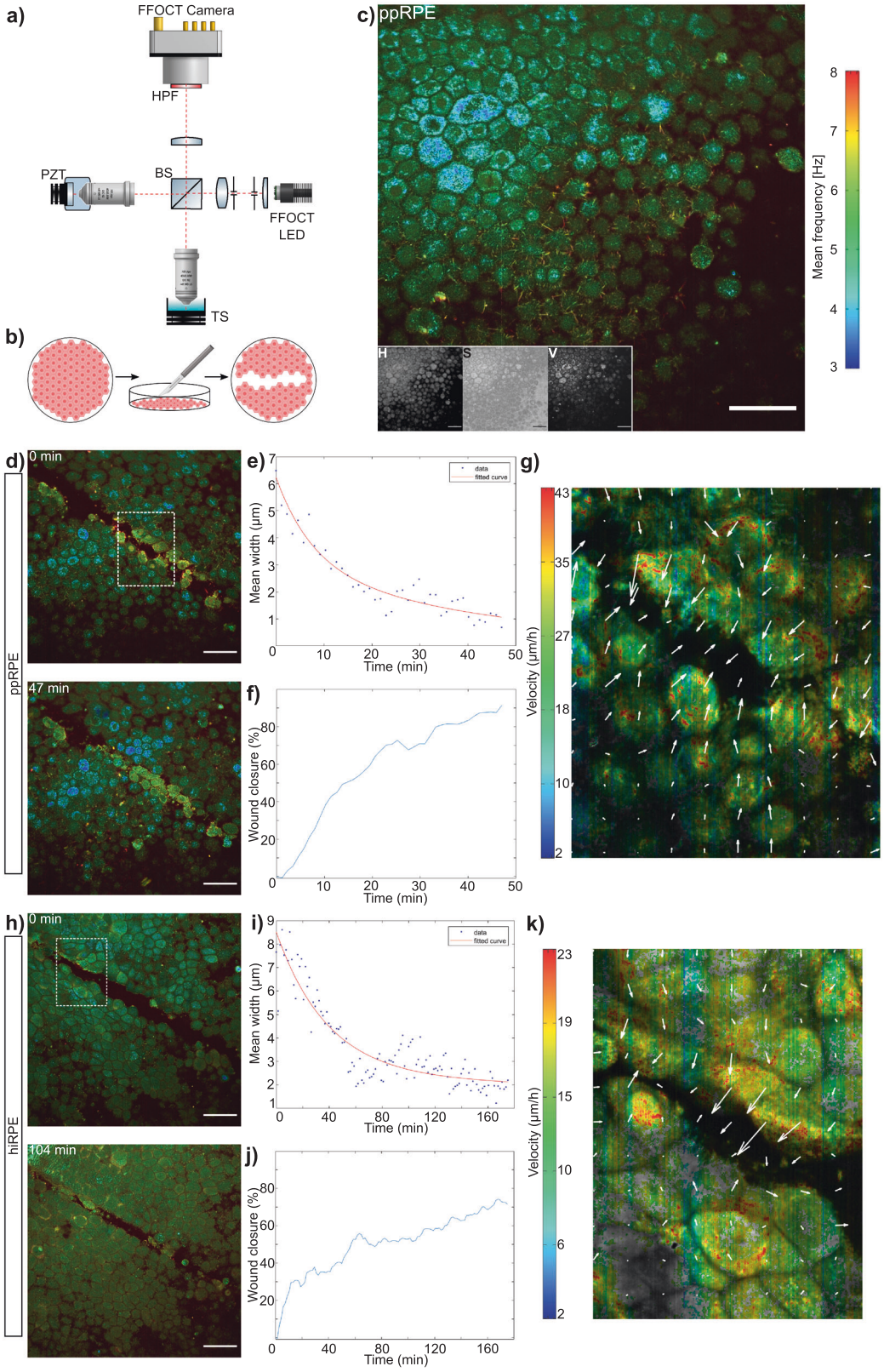
In this article, we propose the use of D-FFOCT to perform non-invasive live imaging of RPE cell cultures. We validate a novel RPE stress model, provide a new tool to quantify RPE wound-healing parameters, and identify the organelles responsible for the D-FFOCT signal.

Results

RPE stress model and quantification methods. Primary porcine RPE cell cultures (ppRPE) ($n = 5$), which have the advantage of being highly pigmented as human mature RPE cells, and human-induced pluripotent stem cell derived RPE (hiRPE) at an early development stage (unpigmented)[14,15] ($n = 9$) were grown on polycarbonate membranes. The setup used for D-FFOCT imaging is shown in Fig. 1a. We followed the evolution of the RPE cell cultures over periods from 1 to 6 h (3 h on average) of D-FFOCT live imaging after inducing stress. Stress was created by performing a scratch assay on the cell layer with a scalpel blade, allowing us to generate a focal and easily reproducible stress damage to the epithelium as shown in Fig. 1b (see the "Methods" section). Figure 1c shows a D-FFOCT image of an intact ppRPE sample with the corresponding colorbar, where the three channels H, S and V of image processing (see the "Methods" section) are represented in the lower left corner. Sets of parallel cultures were imaged at fixed timepoints with immunohistochemistry (an histology technique using bio-engineered antibodies coupled with fluorescent probes to stain specific proteins and cellular structures within tissues), in order to identify the organelles generating the D-FFOCT signal.

Depending on the origin of the cells (ppRPE or hiRPE) and the width of the scratch, cell behaviours differed. Two main features are usually used to quantify wound healing: the speed of closure, i.e., the evolution of the width of the scratch, and the wound closure, measuring the evolution of the area of the scratch[16]. Semi-automatic segmentation based software, named scratch assay velocity evolution (SAVE) profiler (see the "Methods" section), was developed to segment the wound and calculate the width and area of the scratch in order to quantify wound closure. Our SAVE Profiler method outperformed the reference methods using optical flow calculations[17] and the Cell Profiler using the Wound Healing example[18].

RPE behaviour observed after stress. In this RPE stress model, we separated three cases: scratches inferior to 25 µm wide (Fig. 1), scratches between 25 and 100 µm (Fig. 2 and Supplementary Fig. 3), and scratches superior to 100 µm (Supplementary Fig. 1). Figure 1 shows wound closure on both ppRPE (Fig. 1d–j) and hiRPE (Fig. 1h–k) cell cultures for scratches smaller than 25 µm. In a ppRPE sample, after 47 min, the wound was completely closed (Fig. 1d) (see the whole acquisition in Supplementary Movie 1). Calculations of scratch assay evolution were made over a small area (white dotted square on Fig. 1d) to reduce calculation time. Figure 1f plots the wound closure, which represents the evolution of the wound area, as calculated with the SAVE profiler. A quasi-complete closing was achieved, with the wound closure reaching over 90% during the acquisition. Figure 1e represents the evolution of the mean scratch width (blue points). This evolution could be fitted with a double exponential $f(x) = a \times \exp(b \times x) + c \times \exp(d \times x)$. The characteristic time of closing obtained with this fit was approximately 18 min. The closest distance of closing of around 1 µm was reached after 23 min, corresponding to the average interstice between cells which is not affected by the scratch. As the time of closing is dependent on the size of the wound at the beginning of the acquisition, we decided that it was more representative to calculate the speed of closing. Average wound closing speed for this ppRPE sample was thus calculated to be 15.7 µm/h. Figure 1g presents an optical flow calculation over the same area. The velocity of movements throughout the acquisition is shown, with two fronts of motion in opposite directions revealed by the arrows. By averaging the velocities (i.e., the absolute values without taking the direction into account) plotted in Fig. 1g, the medium speed of one front can be calculated as 8.25 µm/h. As there are two opposite moving fronts, the total velocity of closing is the multiplication of the average speed of one front by 2, giving a total speed of 16.5 µm/h. This result is consistent with the results obtained with our custom-written SAVE profiler software. The same analysis was performed on hiRPE cell cultures (Fig. 1h–k) (see the whole acquisition in Supplementary Movie 2). Figure 1h shows the cell layer, almost closed, 103 min after the first image was acquired. The white dotted square on (Fig. 1h) represents the area over which calculations were performed. The wound does not completely close (Fig. 1h), reaching an average wound closure of 70% (Fig. 1j). As for the ppRPE scratch assay, the mean scratch width was plotted in Fig. 1i, where it could also be plotted with a double exponential. In this case, the characteristic time of closing was



around 55 min, and an average limit of 2.5 µm was reached after approximately 60 min. The average speed of closing was therefore 6.5 µm/h. The results of the optical flow method are shown in (Fig. 1k), clearly showing two borders which progress in two different directions, but the upper border is more active than the lower (see the aspect of arrows in Fig. 1k. The average speed calculated on the optical flow representation was 4.05 µm/h, and by multiplying this result by 2 to be cohesive with two different borders, we obtain 8.1 µm/h, consistent with the results of the SAVE profiler. The optical flow results show that the whole cell layer is moving in order to close the wound, with a higher speed for the first row of cells. The SAVE Profiler was validated on the Wound Healing example of Cell Profiler. Cell Profiler showed less effective segmentation (Supplementary Fig. 2b) for the hiRPE

Fig. 1 D-FFOCT imaging and scratch techniques, results of closing (<25 µm) scratch assays. a Drawing of our custom-built Full-Field OCT system. BS beam-splitter, HPF high-pass filter, PZT piezo-electric translation, TS translation stage (for the sample). **b** Schematic of the RPE cell layer before and after the scratch assay (from left to right). **c** Recombined three channels of HSV computation and the three different channels in lower left. The colorbar represents the frequency variations of the sample (Hue channel). **d**–**g** Results of the analysis of a closing scratch assay on a primary porcine RPE cell culture (ppRPE). **d** Beginning and end (i.e., closing) of the imaging of the scratch assay. The dotted white square corresponds to the area used for calculations. **e**, **f** Plots of the evolution of scratch width and wound closure over the acquisition, calculated with SAVE Profiler. **g** Optical flow calculations showing velocity and motion direction. **h**–**k** Results of the analysis of a closing scratch assay on a hiRPE cell culture. **h** Beginning and end (i.e., closing) of the imaging of the scratch assay. **i**, **j** Plots of the evolution of scratch width and wound closure over the acquisition, calculated with SAVE Profiler. **k** Optical flow calculations. (Statistics: see Supplementary Table 1) (scale-bar: 50 µm).

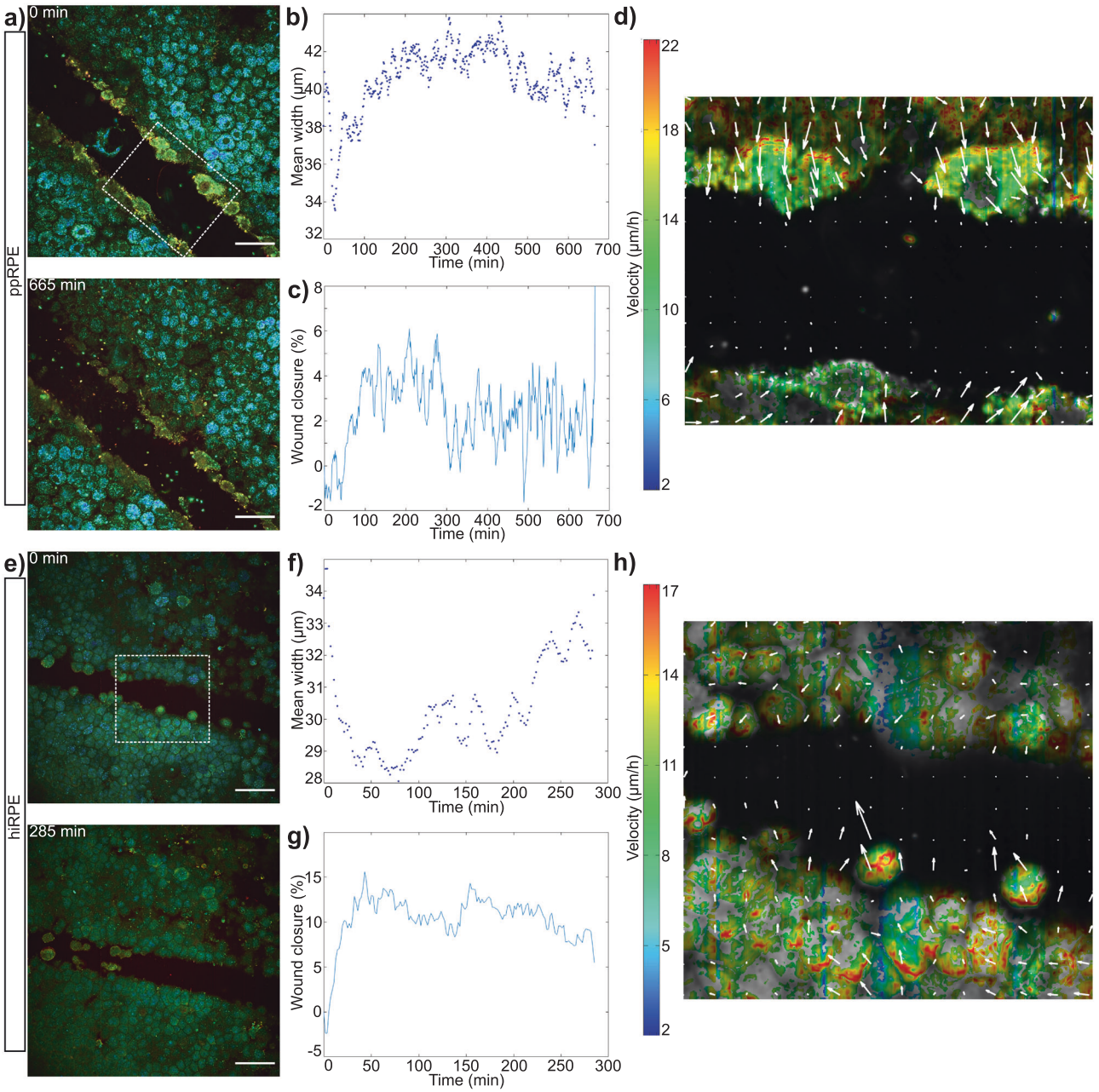


Fig. 2 Results on scratch assays (>25 µm) on ppRPE and hiRPE cell cultures, failing to close entirely. a Beginning and end of the imaging of a scratch assay on ppRPE cell culture. **b**, **c** Evolution of scratch width and wound closure calculated with our programme and **d** optical flow calculations. **e** Beginning and end of the imaging of a scratch assay on hiRPE cell culture. **f**, **g** Evolution of the scratch width and wound closure, calculated with the SAVE profiler and (**h**) optical flow calculations. (scale-bar: 50 µm) (Statistics: see Supplementary Table 1).

sample and (d) for the ppRPE sample) as it does not uniquely target the wound, compared to our SAVE Profiler segmentation shown in Supplementary Fig. 2a and b for the same samples. The Cell profiler results of wound closure (in Supplementary Fig. 2b and d) are therefore not consistent with our observations. Moreover, SAVE profiler was twice as fast as Cell Profiler.

As the scratch assays were performed manually with a scalpel blade, the initial width of the wound could vary. In wounds sized between 25 and 100 µm, the wound failed to close. Fig. 2 presents failure of wound closure on wounds of greater than 25 µm width in ppRPE and hiRPE. In ppRPE (Fig. 2a) (see the whole acquisition in Supplementary Movie 3), the first and the last images of the acquisition are 665 minutes apart. Calculations were performed over the area in the white dotted square. The evolution of the scratch width (Fig. 2b) and the wound closure (Fig. 2c) show that the cell layer first tends towards closure for the first 30 min with a speed of 15 µm/h, followed by a period of retraction. Figure 2d presents the results of the optic flow calculations: the arrows show an initial movement towards wound closure, but the inside of the wound remains stationary, in contrast to wounds under 25 µm size in Fig. 1. hiRPE generally showed similar behaviour (Fig. 2e–h) (see the whole acquisition in Supplementary Movie 4), with an attempt to close at a speed of 8.3 µm/h for the first 40 min. Two cells appear with a higher velocity: these cells were dying and detached from the border of the wound. Cell Profiler was more effective on non-closing than on closing wounds and gave consistent results with those calculated with SAVE Profiler (see Supplementary Fig. 3). It is interesting to note that the wound closure attempt in larger wounds had a similar speed as the successful closure of small wounds presented in Fig. 1. Despite slightly different results of wound closure speed, the overall observed behaviours were the same in both ppRPE and hiRPE samples, beginning with an attempt at closure, followed by retraction.

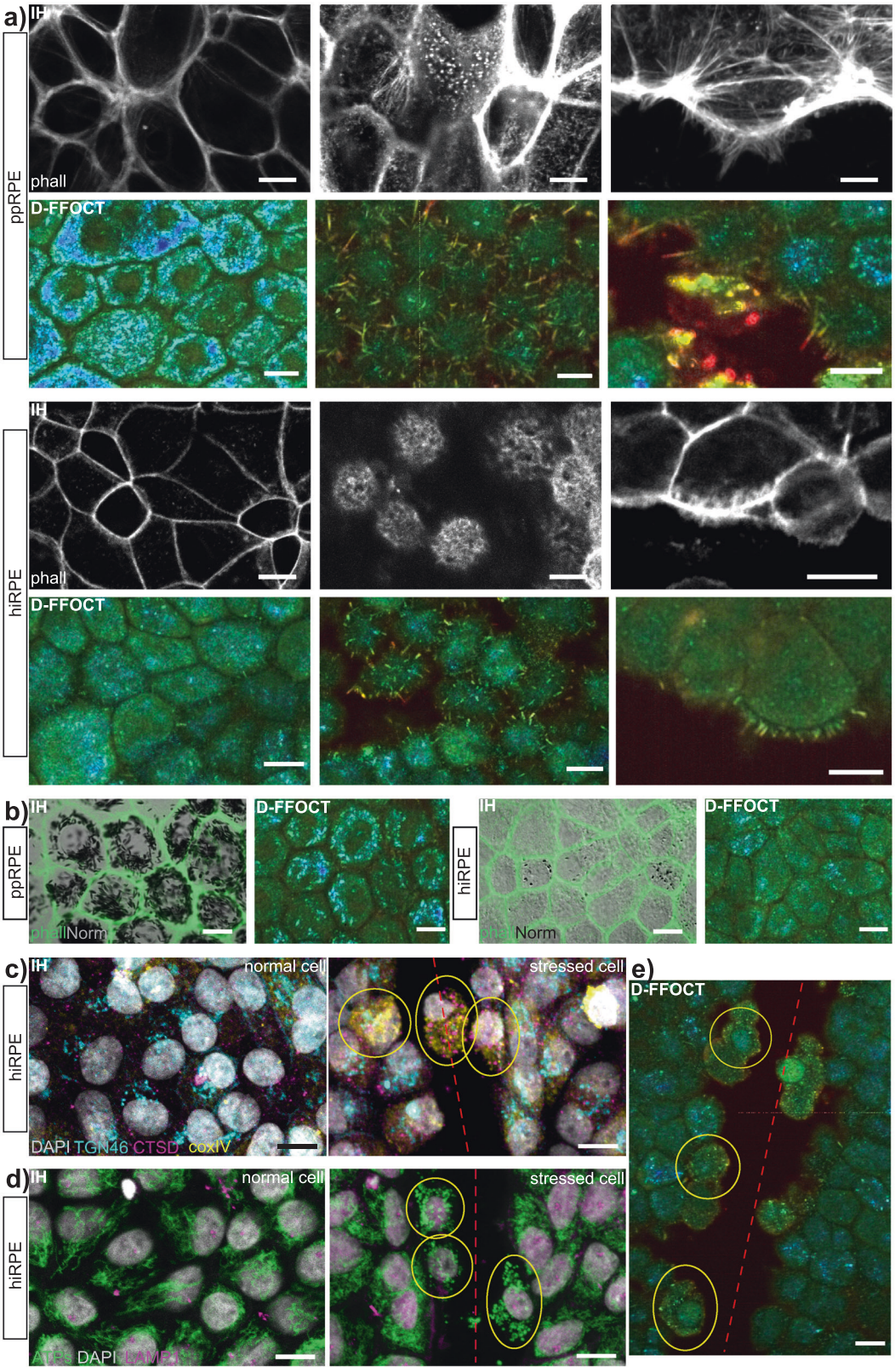
In summary, small wounds (under 25 µm) lead to a repair of the damaged cell layer, while large wounds (between 25 and 100 µm) tend to create a movement towards closure followed by a retraction. For wounds larger than 100 µm, we observed a direct expansion of the cell layer with no evidence of attempt at closure as shown in Supplementary Fig. 1 (see Supplementary Movie 5). Comparing repair processes for the two types of RPE cells, ppRPE tend to close faster, with a mean speed between 15 and 18 µm/h, while hiRPE close with a speed between 3 and 8 µm/h. Moreover, ppRPE tend to reach a wound closure of almost 100%, while for hiRPE this is not always the case. We eliminated membrane coating as the source of the difference by imaging hiRPE samples grown on both uncoated and coated membranes with similar results. The reasons for the differences may be both species-related and culture method-related, as ppRPE is a primary culture while hiRPE is a cell differentiation. The statistics of the scratch assays performed are compiled in Supplementary Table 1.

Validation of D-FFOCT signal with immunohistochemistry. In D-FFOCT images, the dynamic profile of the cells around the border of the scratch evolve throughout the acquisition. In order to understand which organelles were involved in these phenomena, ppRPE and hiRPE scratch assays and wound healing observed over a period of several hours with D-FFOCT were paralleled by a set of identical cultures fixed at different timepoints for immunohistochemistry validation, via fluorescent labelling of different organelles. Actin filaments (labelled using a high-affinity F-actin probe conjugated to fluorescent dye, (Fig. 3a) contribute to the cytoskeleton of the cell in varied cell structures in RPE: the cell cortex (first column of Fig. 3a), the microvilli (second column of Fig. 3a and Supplementary Fig. 4b and c, labelled with ezrin that specifically targets the microvilli[14,19,20]) and the fillipods (last column of Fig. 3a). The cytoskeleton includes the cortex sustaining the plasmic membrane, which is static, while the microvilli and the fillipods are both very active. As the cortex is static, it appears black on D-FFOCT images, while microvilli and fillipods were very active: moving rapidly and constantly (high intensity and red) in D-FFOCT. Individual microvilli were easily visible at the surface of RPE cells on D-FFOCT images compared to immunohistochemistry images, and could be imaged in 3D by performing a stack acquisition in depth. Their movement could be followed through live image sequences using a custom GPU-computing software (Holovibes http://holovibes.com/[21], see Supplementary Movie 6), for the first time to our knowledge. After a closed scratch assay, an accumulation of actin is visible in immunohistochemistry (Supplementary Fig. 4a). It is composed of the border cells of the wound which seem to disintegrate after the closing, as observable in the corresponding D-FFOCT image. This is coherent with the literature[22]. It was also observed that apical processes along the wound border are lost a few days after a scratch assay (Supplementary Fig. 5).

Pigment particles (ovular, 2–3 µm × 0.5–1 µm) absorb light, making them visible in conventional microscopy and phase contrast microscopy (here we used Normarski interference contrast and superimposed the fluorescent phalloidin image corresponding in green as reference image). They were individually resolved throughout the D-FFOCT images in Fig. 3b. As primary cultures, ppRPE were highly pigmented, while hiRPE contained little pigment. Pigment was active but very slow moving, giving a bright blue dynamic profile in D-FFOCT. The ovular shapes measured around 3 µm × 1 µm, corresponding to the literature[10]. The difference in pigment signal between ppRPE and hiRPE is highly visible (Fig. 3b). This assumption was confirmed by phase contrast microscopy of the samples, showing a large difference in melanin concentration.

The dynamic profile was different for cells far from the wound and for cells close to the wound (Fig. 3e). The main parameter that changes in the dynamic profile was the colour, meaning the frequency of sub-cellular movements.

Golgi apparatus (cyan label) showed a uniform distribution and activity across all cells, regardless of cell damage or wounding in Fig. 3c. Golgi therefore contributed evenly to the D-FFOCT signal throughout the sample. Lysosomes (magenta label in Fig. 3c and d, using two different antigens for confirmation), vesicles that contain hydrolytic enzyme and act as the waste disposal system of the cell, were visible in a small proportion of cells which detached from the culture and became mobile. Their high activity and mobility during late apoptosis caused them to have a bright red dynamic profile in D-FFOCT, and they tended to migrate toward the wound during closure. In cells neighbouring the wound, mitochondria (yellow label in Fig. 3c and green label in Fig. 3d, using two different antigens for confirmation) change aspect in the cells circled in yellow on stressed cell images. Therefore, we can affirm that mitochondria are involved in D-FFOCT signal. To go further in this observation, we compared immunohistochemistry imaging of mitochondria to D-FFOCT images at four different timepoints (0, 1, 2 and 3 h) on both normal cells and stressed cells in Fig. 4a. While the mitochondria organisation in immunohistochemistry and their dynamic profile in D-FFOCT were identical over time for normal cells, we observed that mitochondria change form from a filament network to isolated round spheroids in stressed cells (two right columns), which is coherent with the literature[23–25]. These changes were visible in D-FFOCT thanks to their form, their high activity revealed by their colour changing from green to red, and their enhanced brightness. As the resolution of D-FFOCT is 0.5 µm,



healthy individual mitochondria (diameter 0.4 µm) were not resolved but gave a general background signal, while the bright dots in stressed cells suggest that they are damaged mitochondria which formed larger spheres that could be individually distinguished[24,25]. This behaviour disappears a few days after the scratch assays (Supplementary Fig. 5b): cells on the border of the wound no longer appear bright and the dynamic profile of the entire cell sheet is similar to that of unstressed cells. In order to further validate the expression of stress in D-FFOCT images, hiRPE cell cultures were also tested under oxidative stress (see the "Methods" section for protocol) which creates a mitochondrial stress. Parallel sets were analysed in D-FFOCT, Immunohistochemistry (ATPs staining) imaging and live imaging (MitoTracker). The results are shown in Fig. 4b. First, three images

Fig. 3 Immunohistochemistry validation of organelles. Nuclei were labelled with DAPI. Red dashed lines show the scratch direction. **a** Actin filaments (phalloidine in IH) validation on ppRPE and hiRPE. The left column shows the cell cortex (static) appearing dark in D-FFOCT. The centre column presents microvilli. Their visualisation is easier in D-FFOCT: they appear as red cillias on top of RPE cells. The right column shows filipods on the side of the cells close to the wound, appearing in red in D-FFOCT such as microvilli. (The IH images for filipods were taken at slightly different depths, showing more stress fibres for ppRPE). **b** Comparison of pigment granules on both ppRPE (highly pigmented) and hiRPE (few pigments). Actin filaments (cytoskeleton) are labelled with phalloidine in IH, while pigments were imaged with phase contrast imaging (Normarski). **c** Golgi apparatus (TGN46 in cyan), lysosomes (CTSD in magenta) and mitochondria (coxIV in yellow) IH comparison between normal cell and stressed cell (circled in yellow). **d** Mitochondria (ATPs) and lysosome (LAMP1) validation in IH between normal cell and stressed cell (circled in yellow). **e** Related D-FFOCT image for (**c**) and (**d**) showing both normal cells and stressed cells (circled in yellow). IH: immunohistochemistry (scale-bar: 10 μm).

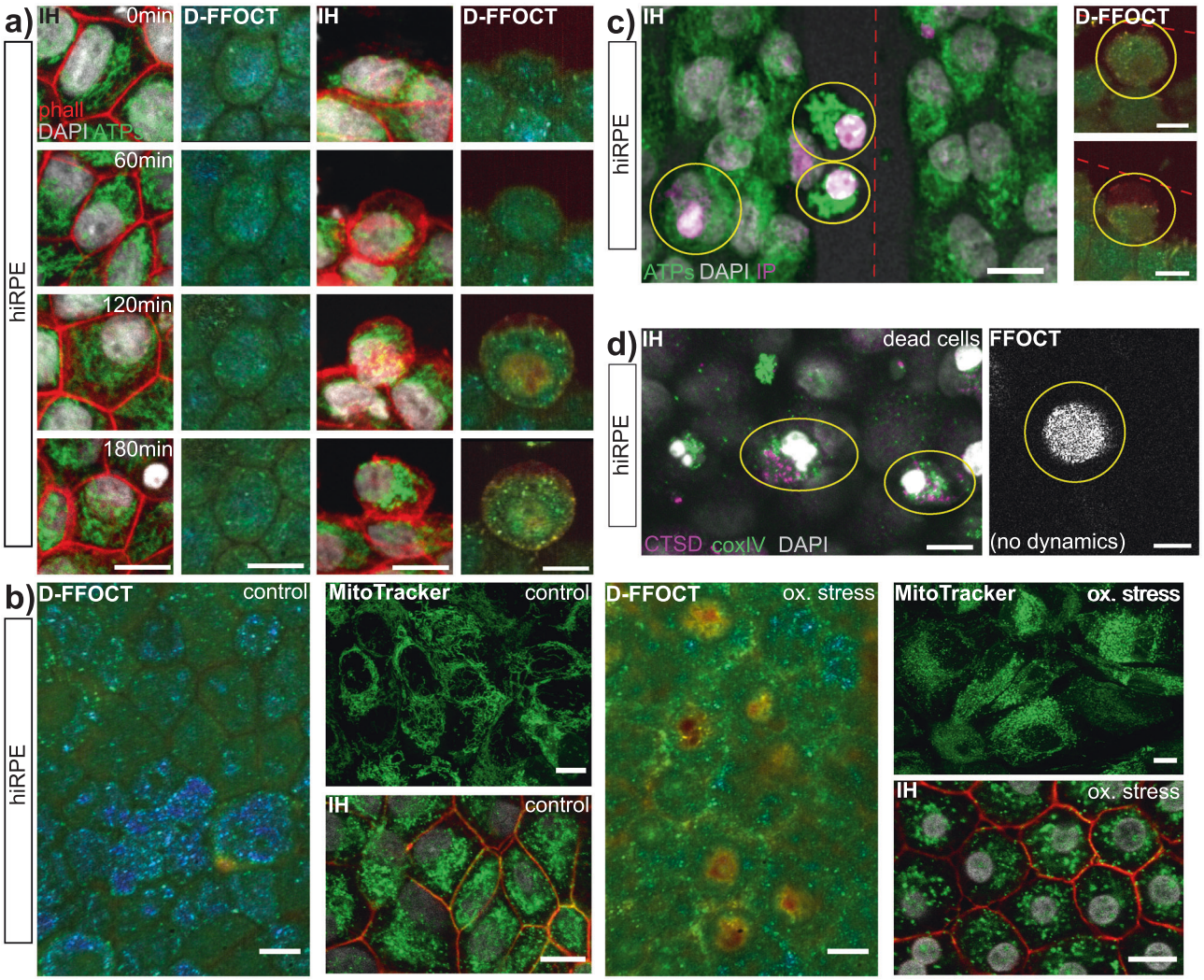


Fig. 4 Cell phenotypes. Nuclei were labelled with DAPI. Red dashed lines show the scratch direction. **a** Mitochondria phenotype evolution over 3 h. The two left columns show the evolution of a normal cell, with a constant phenotype. The two right columns present the evolution of a stressed cell, with changes in mitochondria aspect (IH) and in dynamic profile (D-FFOCT). **b** Mitochondria phenotype evolution following an oxidative stress. The left three images show control samples in dynamic profile (D-FFOCT) and both IH (ATPs staining) and live fluorescence imaging (Mitotracker). The right three images show samples after oxidative stress with the same imaging methods. The D-FFOCT image shows a brighter and faster dynamic profile after stress (i.e., red in the nuclei, green to yellow in the cytoplasm, in addition to the pigment (blue) seen in both control and stress cases). Both IH and Mitotracker show fragmented mitochondria. **c** Dying cells (circled in yellow) 2 h after the scratch, labelled with propidium iodide (IP in magenta), showing a condensed nucleus. Mitochondria are labelled with ATPs (green). Corresponding cells in D-FFOCT on the right. **d** Dead cells (circled in yellow) floating over the cell culture. Lysosomes labelled with CTSD (magenta), mitochondria with coxIV (green) in IH. Corresponding cells do not exhibit any dynamic signal and are only visible in static (structural not functional) FFOCT. IH immunohistochemistry (scale-bar: 10 μm).

show the control cultures. The D-FFOCT image shows a uniform cell layer exhibiting a blue-green dynamic signal. Both immunohistochemistry and MitoTracker images show mitochondria organised in a network, meaning no stress is visible in the cells. The last three images show the results on a parallel set of cell cultures after 4 h of oxidative stress. The cells present in the D-FFOCT image show changes in the dynamic profile: the cells are green to yellow and brighter while the nuclei appear bright and red (i.e., larger and faster subcellular movements), indicating that the cells are undergoing stress. Small bright dots are also

visible, as in Fig. 4a for the D-FFOCT image 180 min after scratch stress. These results are cohesive with the immunohistochemistry and MitoTracker images, showing damaged mitochondria (uncoupled) and condensed nuclei.

Dying cells are distinguishable in D-FFOCT. Cells undergoing apoptosis or necrosis were labelled with propidium iodide (magenta label) in Fig. 4c. These cells (circled in yellow) show a condensed nucleus and a change in mitochondria organisation (green label), thus undergo apoptosis. In D-FFOCT, these cells appear with a faster subcellular activity (red dynamic profile) and a condensed nucleus with also a higher activity. The size of nuclei were measured and compared in both imaging techniques and the results were consistent (diameter under 7 µm for condensed nuclei). However D-FFOCT signal is not related to dead cells: those few cells which died (showing a high concentration of lysosomes in magenta label) following apoptosis and remained mobile in the cultures are dark in D-FFOCT due to absence of organelle activity (Fig. 4d), but the structure is visible in static FFOCT, recorded in parallel, which reveals static structural rather than functional information.

Our results are confirmed by those shown in literature with electron microscopy[10], where the RPE cytoplasm is mainly filled with mitochondria (usually arranged in a network for unstressed cells) and pigment granules (of similar size to those measured here with D-FFOCT). Electron microscopy of microvilli, shown in the same paper[10], is also consistent with what we observed with D-FFOCT, but is not capable of showing the movements that were visible with D-FFOCT.

Discussion

D-FFOCT is able to non invasively show mitochondrial dynamics, microvilli and fillipods, and pigment distribution in RPE cells via live imaging in real time. Comparison of wound healing parameters quantified using optical flow[17], semi-automatic segmentation methods (SAVE Profiler) and Cell Profiler software[18], showed that our custom-developed SAVE Profiler successfully combines results from both optical flow and Cell Profiler in a shorter calculation time. Wound healing parameters such as speed agreed with the literature[26]. In our experiments (between 1 and 6 h), we only saw migration of cells especially for small wounds, which is coherent with Hergott et al.[26], while large wounds tend to involve proliferation. Moreover, we saw that the integrity of the membrane was important for the closing of the wound as shown in Geiger et al.[22]. Jacinto et al.[27] and Farooqui et al.[28] show that several rows of cells participate in the closing of the wound. This phenomenon was observable on closing wounds in D-FFOCT. Filipods seem to also be involved in the closing of the wound, which is confirmed by Jacinto et al.[27]. The different methods presented to calculate the evolution of scratch assays present consistent results on the speed of either closing or expansion. Differences were observed depending on the origin and maturation stage of the sample, in accordance with the literature[16]. The experiments were performed multiple times ($n = 5$ ppRPE; $n = 9$ hiRPE) giving the same results each time on speed and wound closure. In small (<25 µm) scratches, wounds closed at 16 µm/h for ppRPE and 5 µm/h for hiRPE on average. After wound closure, the actin remained thickened around the wound, some damaged mitochondria remained encompassed by other cells, and cells along the wound border remained raised above the rest of the culture surface. It was observed that the width evolution seems to follow a double exponential fitting for both types of samples. While we have not demonstrated that this model has a physical basis, a potential explanation could be that each border may move as a simple exponential, moving at its own speed, thus creating a double exponential across the two bordered wound. In wounds with large scratches (>25 µm), a different behaviour was observed: an initial attempt at wound closure (cell sheet moving inwards) was overcome by a retractive movement away from the wound, with sliding of the whole cell sheet. This behaviour displays some similar characteristics to those seen in vivo over long (several months to years) time periods on patients with geographic atrophy lesions forming[29]. The dynamic profile of cells was also consistent throughout the acquisitions: cells on the border of the wound show a faster (i.e., colour tending to yellow/red) and higher (i.e., brighter) signal than cells far from the wound. These observations on D-FFOCT images were consistent with the results obtained in immunohistochemistry, showing that mitochondria have a different behaviour in the damaged cells, and appear to be the organelles undergoing the most drastic phenotype change. In order to get closer to human in vivo RPE cells, we tried to study hiRPE at a mature development stage (pigmented, 90 days of growing). Unfortunately, we were not able to determine if the cell movements were due to the scratch assay or breaks in the cell layer caused by lack of membrane adhesion. This problem was also observed by Abu Khamidakh et al.[16]. Future developments of this study would be to automatise the realisation of scratch assays with a new setup combining a laser to cut the cell layer with better repeatability. We could also test the addition of molecules to change the speed of closure[30]. We showed that D-FFOCT combined with custom-developed calculation software allow imaging and study of degeneration in RPE cell cultures, which may contribute to the comprehension and the following of in vivo degenerative retinal diseases (such as AMD) evolution, and could be an appreciated method for live patient diagnostics and direct treatment choice in the future. As a marker of mitochondrial dynamics and fragmentation and thus of their activity[25], D-FFOCT may also be used in the understanding of optic nerve disease, where mitochondria are implicated. Parallels of wound healing or wound retraction in the RPE layer are found with in vivo adaptive optics imaging of AMD patients over year long periods[31]. D-FFOCT shows potential to address current limitations of in vitro cell culture models for applications like disease modelling and drug screening due to its non-invasive 3D live imaging performance over periods from minutes to days. This presents, for the first time, the opportunity to follow up a single culture during the processes of disease development or therapeutic effect without the approximation involved in current practice of the use of multiple cultures sacrificed at multiple time points. This could positively impact the robustness of outcome measures of future disease models and therapeutic trials in the in vitro culture setting.

Methods

Dynamic full-field OCT: experimental setups and image processing. Optical coherence tomography (OCT) is an imaging technique which allows non invasive scanning of a sample in depth, invented in 1991[32]. Time-domain full-field OCT (FFOCT)[33–35] is an interferometric imaging technique which is an *en face* variant of OCT. This configuration, based on a Linnik interferometer, i.e. an OCT setup with microscope objectives in the reference and sample arms, allows the recording of 2D images on a CMOS camera in a single shot. By scanning the sample in depth, 3D volumes of the structure of the sample can be acquired (see Supplementary Movie 7). For our study, we used a laboratory-designed time-domain FFOCT (see Fig. 1a). This setup is composed of a water-immersion microscope objective in each arm (Nikon NIR APO ×40 0.8 NA), giving a lateral resolution of 0.5 µm for a total field-of-view of 320 × 320 µm^2. The axial resolution of 1.7 µm is also determined by the microscope objectives, due to their high numerical aperture. The camera used is an Adimec camera (Quartz 2A750, Adimec), custom-built for our purpose. The illumination is performed by an LED, centred at 660 nm (M660L3, Thorlabs), which is separated into reference and sample arms by a beamsplitter (BS028, Thorlabs). The reference arm is composed of a silicon mirror (to approach a reflectivity match with the biological samples), affixed to a piezo-electric translation stage. The piezo-electric translation stage in the reference arm is used to generate a phase shift. A pair of π-phase shifted images are recorded and substracted to extract the coherent part of the interference signal between the imaged sample plane and the reference mirror.

Recently, we showed that a new type of contrast could be extracted from images acquired with FFOCT[36]. By acquiring several hundred images without using the piezo-electric translation of the reference arm, and calculating the standard deviation over the image stacks, we are able to extract the intrinsic motion of the biological sample. The intrinsic motion is created by the movements of the organelles inside the cells constituting the biological sample[37]. These dynamics are referred to as the "dynamic profile" throughout this article. The image computation of the dynamic profile is based on a power spectrum analysis, as shown in Scholler et al.[9]. For this purpose, 512 images are recorded at 100 Hz on our FFOCT setup. The power spectrum analysis is then performed on each voxel of the stack of images. The study of the time variations over each voxel helps to highlight the intra-cellular motion recorded. These variations are coded in the Hue-Saturation-Value colorspace, which is an orthogonal colorspace, providing us three different channels to compute different physical parameters.

The mean frequency of the recorded intra-cellular motion codes for the Hue channel, which represents the colour in the image. The colour ranges from blue, representing low frequencies, to red, coding for high frequencies. The saturation channel is coded by the inverse of the frequency bandwidth of each voxel. For a broad bandwidth, meaning there is a large range of frequencies, the saturation will be low, creating a greyish appearance. On the contrary, for a sharp bandwidth, where a specific frequency is emphasised, the saturation will be high, creating a vivid colour. Finally, the value, which codes for the intensity in the image, is calculated as the standard deviation over a moving window of 50 images, which are then averaged, to give the final intensity highlighting the intra-cellular motion. Finally, the three channels are combined to create a coloured image, representing the dynamic profile of the imaged sample (see Fig. 1c).

The acquisitions in depth were performed from the top of the cells to the membrane by acquiring D-FFOCT images in stacks with a step of 1 µm. For the timelapse acquisitions, D-FFOCT images were acquired every minute for up to several hours in the same plane, using a plane lock-in stabilisation software previously presented in Scholler et al.[9]. This stabilisation software is based on the cross-correlation between the first image and the current image. Retrieving the first position is made by scanning the sample axially over 10 µm, in order to find the best cross-correlated plane.

RPE cell cultures. Different methods have been developed to grow RPE[38]. We described here the methods used for both ppRPE and hiRPE samples.

Porcine eyes were bought at a local slaughterhouse (Guy Harang, Houdan, France) in agreement with the local regulatory department and the slaughterhouse veterinarians (agreement FR75105131). This procedure adheres to the European initiative for restricting animal experimentation as not a single animal was killed for our experimentation. The eyes were taken from animals sacrificed daily for human consumption. Eyes were cleaned from muscle, and incubated for 4 minutes in Pursept-AXpress (Merz Hygiene GmbH, Frankfurt, Germany) for disinfection. The anterior portion was cut along the limbus to remove the cornea, lens and retina. A solution containing 0.25% trypsin–EDTA (Life Technologies, Carlsbad, CA, USA) was introduced for 1 h at 37 °C in the eyecup. RPE cells were then gently detached from the Bruch's membrane and resuspended in Dulbecco's Modified Eagle medium (DMEM, Life Technologies) supplemented with 20% Foetal Bovine Serum (FBS, Life Technologies) and 10 µg/ml gentamycin (Life Technologies). Purified cells from one eye were pooled and plated in 2 Transwell inserts (reference: 3412 Corning). Cells were allowed to grow in an incubator with a controlled atmosphere at 5% CO_2 and 37 °C. The culture medium was renewed 24 h after the first seeding.

HiRPE were generated using established protocol using AHF1pi2 hiPSC clone as described in Reichman et al.[14]. Thawed hiRPE cells at passage 1 (hiRPEp1) were seeded on Geltrex (Thermo Fisher) precoted flask at 50,000 cells/cm^2 and expanded in the ProN2 medium composed of DMEM/F12, 1% MEM nonessential amino acids, 1% CTS N2 supplement, 10 units per ml Penicillin, and 10 mg/ml Streptomycin; and the medium was changed every 2–3 days. At confluence, hiRPEp2 cells were dissociated using trypsin and replated at 100,000 cells/cm^2 on Gletrex precoted six-well plate (reference: 3412 Corning) for D-FFOCT experiments and in p24 on Gletrex precoted glass inserts for immunostaining. All experiments were done with confluent hiRPEp3. Cells were allowed to grow in an incubator with a controlled atmosphere at 5% CO_2 and 37 °C for 3 weeks.

Choice of sample holder for D-FFOCT imaging and scratch assays. In order to model in vitro degeneration on a RPE cell culture, scratch assays were performed manually with a scalpel blade through the cell layer on the sample holder, immersed in CO_2 independent medium (Gibco). The wounds performed ranged from 10 µm wide to over 300 µm.

Different materials were tested as sample holder for the cells (see Supplementary Table 2 in Supplementary information). The material needs to have three main characteristics: (i) the cells should grow easily on it, (ii) it should have a refractive index close to that of water, in order to avoid fringe artefacts caused by our interferometric technique, and (iii) it should be resistant to scratches made by the scalpel blade. Most commonly, cells are grown in Petri dishes made of polystyrene, where they easily and rapidly grow. However, the refractive index of polystyrene is 1.59, far from the refractive index of water, creating fringe artefacts on the D-FFOCT images. Polytetrafluoroethylene (PTFE) membranes with a refractive index of 1.31 do not create artefacts, but PTFE is very fragile and cells do not grow easily on it. The best compromise was found to be polycarbonate membranes. These membranes have a refractive index of 1.58 but, as they are porous, the water can enter the membrane and artificially reduce the effective refractive index. Moreover, this material is quite resistant to scratches and cells grow more easily on it than on PTFE.

Oxidative stress assay. hiRPEp3 were seeded at 50,000 cells/cm^2 in a Geltrex precoated 96-well, 24-well or 6-well plates (Corning 3412) and cultured for a minimum of 2 weeks in ProN2 medium at 37 °C and 5% CO_2. The oxidative stress protocol was developed in accordance with previous publications[39,40]. For MitoTracker™ Green FM assay, cells in 96-well plates were pretreated with 100 µL of MitoTracker™ Green FM diluted at a concentration of 200 µM for 45 min. After removing the MitoTracker™ Green FM, oxidative stress was generated by the addition of 100 µL/well of ProN2 medium containing 1 mM of H_2O_2 (Sigma) for 4 h at 37 °C and 5% CO_2. After treatment, cells were washed with ProN2 medium and mitochondria integrity was observed with confocal microscopy on non PFA-fixed samples. For immunostaining, cells in 24-well plates were treated with 1 mL of ProN2 medium containing 1 mM of H_2O_2 (Sigma) for 4 h. Following treatment, cells were fixed 15 min with cold solution PFA 4%, PBS 1× for downstream immunostaining. For D-FFOCT imaging, cells in 6-well plates were treated with 4 mL (2 mL in the insert and 2 mL in the well) of ProN2 medium containing 1 mM of H_2O_2 for 4 h. Cells were then washed with PBS before being imaged with D-FFOCT in cell culture medium.

Immunochemistry preparation and imaging. To allow both immunohistochemistry and observation of cells using confocal microscopy, parallel sets of hiRPE and ppRPE cells were cultured on glass inserts (as polycarbonate membranes do not permit confocal imaging of the epithelium). To obtain samples similar to D-FFOCT observations, scratch assays were performed on hiRPE and ppRPE cells, followed by tissue fixation using paraformaldheyde 4% at various timepoints: 0 (fixation just after performing the scratch), 60, 120, 180 min and 24 h. Propidium iodide staining was performed using a pre-fixation incubation of the samples for one hour at 37 °C before cell fixation. Immunostaining was performed using the following solution: PBSGT, 1× PBS containing 0.2% gelatin: 24350262, Prolabo, and 0.5% Triton X-100 T8787, Sigma Aldrich. A first incubation of the tissues with PBSGT alone for 2 h (at room temperature, with shaking at 70 rpm) allowed blockage of non-specific binding and permeabilization. The cultures were then incubated with the primary and secondary antibodies, in the same PBSGT added with corresponding antibodies, at 4 °C overnight for the primary antibody and the secondary antibody.

Different organelles were labelled using the following primary antibodies:

- Mitochondria: ATP synthase Subunit Beta Mouse Monoclonal Antibody (A21351 Life Technologies) 1/500 and mCoxIV (mouse monoclonal [20E8] ab14744 Abcam) 1/250
- Nuclei: Hoescht 1/1000
- Actin filaments: phalloidin 1/40 (10634053 Fisher Scientific)
- Microvilli: ezrin 1/250 (Sigma-Aldrich Cat# E8897)
- Lysosomes: LAMP1 (ab24170 Abcam) 1/500 and CTSD (sc6486 Santa Cruz) 1/150
- Golgi apparatus: TGN46 (rabbit polyclonal ab50595 Abcam) 1/250
- Dying cells: propidium iodide (P4170, Sigma Aldrich) 1/1000

Fluorescent secondary antibodies were produced in donkey, against rabbit, goat, and mice and coupled with Alexa 488 and 594 (1/500, Sigma aldrich).

After immunostaining, samples were then mounted in Vectashield (H1000, Vector Laboratories). All images were acquired with a confocal microscope, with an oil immersion objective (classical imaging) using either confocal fluorescence imaging or Normarski phase contrast imaging mode. Images were observed and processed with FIJI[41].

The SAVE profiler: custom-developed software to segment and analyse wound closure. In order to evaluate the movement of the cells following the scratch, we wished to study the speed and the percentage of closure of the wound by directly measuring the size of the wound over a time-stack of images. For this purpose, custom software was developed in Matlab, which we name the scratch assay velocity evolution (SAVE) profiler[42].

The first step is to segment the scratch to create a binary image of the scratch and the cells. In order to obtain the best binary image (i.e., which considers the cell interstices, which are not associated with the scratch, as part of the cells), we applied a multiple threshold to the image and retained only the first level, which separated the scratch from the rest of the image. We performed this multiple thresholding on the first and the last images of the stack, as the intensity level in the images can change during an acquisition. As we thus obtain two different threshold levels, we smooth the threshold linearly throughout the stack of images.

The second step is to facilitate the calculation over the scratch. The user is asked to draw a line along the scratch, helping to evaluate the direction of the scratch. The images are then rotated to have the scratch placed vertically on the images.

We then remove any remaining pixels which do not belong to the scratch by drawing an approximate contour of the wound, which is applied to all of the images. If the scratch is closing, the contouring is done on the first image (as it is on this image that the scratch is the largest). For an expanding scratch, the contouring is done on the last image. The images are also resized to crop the edges of the images before rotation.

The stack of images is finally ready for calculation. First, we calculate wound closure[43], which evaluates the evolution of the area of the scratch over the acquisition period. The area is calculated on each frame by counting the pixels contained within the region of the scratch. The formula of the wound closure is: $\frac{\mathrm{area}(t=0)-\mathrm{area}(t)}{\mathrm{area}(t=0)} \times 100$, giving a percentage of closure or expansion.

Secondly, we calculate wound size evolution. The width of the scratch is calculated by counting the pixels in each row of the image (as the scratch is oriented vertically, the width corresponds to an horizontal line, i.e., a row). Then, for each frame, we calculate the maximum and the minimum widths, but also the mean width. The mean width was plotted over time and fitted with a bi-exponential function, determining the characteristic time and the speed of closing. The limit of closing was fixed at around 1–2 µm, which is the average interstice between cells far from the wound.

We validated our custom developed SAVE profiler software against an existing software. Cell Profiler is a cell image analysis software developed in 2005[18]. We used the Wound Healing example available on the website https://cellprofiler.org. By analysing images of a healing wound over time, this software calculates the area occupied by the cells on each image. Thus, we were able to calculate the wound closure (formula explained above) in order to compare with the results obtained with our SAVE profiler. We observed that Cell profiler was efficient on non closing wounds (i.e., failure of closing and expansion) and gives similar results. However, the segmentation performed by Cell profiler on closing wounds was incomplete (as shown in Supplementary Fig. 2b and d) as it takes into account the differences of intensity in the images, misrepresenting the results of wound closure. Moreover, calculation time using Cell Profiler is considerably extended for long acquisitions (e.g., twice as long for more than 150 images), compared to our SAVE profiler.

Optical flow. Optical flow is a method to study the motion between frames of a video. It relies on changes in the brightness pattern throughout an acquisition, and is used in navigation control and robotics, or Artificial Intelligence for example. We decided to use the Optical flow method in order to validate the movement and speed evolution imaged with D-FFOCT and calculated with our SAVE Profiler. Here, we first take the intensity channel of the images of an acquisition and apply a median filter to remove noise (e.g., line noise from the camera). We average 8 by 8 frames to improve the intensity and reduce the time of calculation. Then, we apply the Optical Flow from Matlab[8], using the Horn–Schunck method[17]. The Horn–Schunck method is based on the derivatives of the brightness of the frames, assuming there is a certain smoothness in the flow between the images. The optical flow gives magnitude, orientation, and the velocity components on x and y axes.

For the representation of the velocity and the angle of the optical flow, we choose a limit of 2 µm/h as a minimum velocity. The angle is plotted by summing all the different angles calculated through the optical flow process. Velocity is plotted from the magnitude using the quiver function from Matlab, which gives a representation of the velocity with arrows oriented in the direction of the movement and with a length proportional to the velocity (e.g., a higher speed means a longer arrow). Note that optical flow calculations tend to emphasize the inherent row noise of the camera and create sparse line artefacts along camera pixel columns on the velocity representation image. These artefacts are however not present in the original D-FFOCT images and are ignored when concluding on cell velocity.

D-FFOCT and immunochemistry comparison. D-FFOCT has already been shown as a way to distinguish different states of a cell. In Scholler et al.[8], it was shown that, while comparing FFOCT and D-FFOCT images of cell cultures, we can differentiate living cells from dying or dead cells, as these cells show a different dynamic profile. In Scholler et al.[9], we showed that dead cells can be identified from D-FFOCT images alone. Also, different cell types (RPE, photoreceptors, inner retinal neurons) were shown to be distinguishable with D-FFOCT alone.

In this article, we wished to identify the specific organelles responsible for D-FFOCT signal generation, and hence compared to immunohistochemistry.

Statistics and reproducibility. The scratch assay experiments were performed multiple times. The number of samples used are given in Supplementary Table 1. As explained above, a parallel set of both control and scratched samples was used for immunohistochemistry experiments (hiRPE $n = 6$, ppRPE $n = 6$, half control/half scratched, on average). To maximise reproducibility, all scratch assays were performed by the same person (K. Gro.), for both D-FFOCT and immunohistochemistry experiments. For the oxidative stress experiments, 6 samples were used in D-FFOCT (3 control and 3 samples undergoing oxidative stress), samples for MitoTracker live imaging (3 control and 3 stress) and samples for immunohistochemistry imaging (2 control and 2 stress for each condition).

Ethics statement. Porcine eyes were bought at a local slaughterhouse (Guy Harang, Houdan, France) in agreement with the local regulatory department and the slaughterhouse veterinarians (agreement FR75105131). This procedure adheres to the European initiative for restricting animal experimentation as not a single animal was killed for our experimentation. Eyes were taken from animals sacrificed daily for human consumption.

Human induced pluripotent stem cell (hiPSC) derived-RPE cell were generated at the Vision Institute (Paris, France) using established protocol using AHF1pi2 hiPSC clone as described in Reichman et al.[14]. In accordance with French legislation, we certify that the elements or products of the human body or their derivatives obtained have been sampled and/or collected with the prior consent of the donor and that no payment of any form has been provided to the donor for this sample. Handling of donor tissues adhered to the tenets of the Declaration of Helsinki of 1975 and its 1983 revision in protecting donor confidentiality.

Reporting summary. Further information on research design is available in the Nature Research Reporting Summary linked to this article.

Data availability

No datasets were used in this study. All data are displayed in figures, Supplementary figures and Supplementary movies. Supplementary movies are available at this address https://zenodo.org/record/5894962[44]. All data shown in this study are available upon request with K. Gri. (kategrieve@gmail.com).

Code availability

The code used for FFOCT and D-FFOCT acquisitions is available at this address https://zenodo.org/record/3137246[45]. Codes used for the analysis of D-FFOCT acquisitions are available at this address https://zenodo.org/record/5820201[42].

Received: 22 July 2021; Accepted: 11 May 2022;
Published online: 10 June 2022

References

1. Strauss, O. The retinal pigment epithelium by Olaf Strauss-Webvision. In *Webvision-The Organization of the Retina and Visual System*, webvision edn. https://webvision.med.utah.edu/book/part-ii-anatomy-and-physiology-of-the-retina/the-retinal-pigment-epithelium/ (2013).
2. Bonilha, V. L. et al. The retinal pigment epithelium apical microvilli and retinal function. *Adv. Exp. Med. Biol.* **572**, 519–524 (2006).
3. Boulton, M. & Dayhaw-Barker, P. The role of the retinal pigment epithelium: topographical variation and ageing changes. *Eye* **15**, 384–389 (2001).
4. Besch, D., Jägle, H., Scholl, H. P. N., Seeliger, M. W. & Zrenner, E. Inherited multifocal RPE-diseases: mechanisms for local dysfunction in global retinoid cycle gene defects. *Vis. Res.* **43**, 3095–3108 (2003).
5. Sparrow, J., Hicks, D. & Hamel, C. The retinal pigment epithelium in health and disease. *Curr. Mol. Med.* **10**, 802–823 (2010).
6. Klein, R. et al. Prevalence of age-related macular degeneration in the US population. *Arch. Ophthalmol. (Chicago, IL: 1960)* **129**, 75–80 (2011).
7. Forest, D. L., Johnson, L. V. & Clegg, D. O. Cellular models and therapies for age-related macular degeneration. *Dis. Models Mech.* **8**, 421–427 (2015).
8. Scholler, J. et al. Probing dynamic processes in the eye at multiple spatial and temporal scales with multimodal full field OCT. *Biomed. Opt. Express* **10**, 731–746 (2019).
9. Scholler, J. et al. Dynamic full-field optical coherence tomography: 3D live-imaging of retinal organoids. *Light: Sci. Appl.* **9**, 140 (2020).
10. Thumann G., Dou G., Wang Y. and Hinton D. R. Chapter 16 Cell Biology of the Retinal Pigment Epithelium. In *Entokey*. https://entokey.com/cell-biology-of-the-retinal-pigment-epithelium/ (2017).
11. Jensen, E. C. Overview of live-cell imaging: requirements and methods used. *Anat. Rec.* **296**, 1–8 (2013).
12. Toops, K. A., Tan, L. X. & Lakkaraju, A. A detailed three-step protocol for live imaging of intracellular traffic in polarized primary porcine RPE monolayers. *Exp. Eye Res.* **124**, 74–85 (2014).
13. Rathnasamy, G., Tan, L. X. & Lakkaraju, A. Live-cell imaging of mitochondrial dynamics in the retinal pigment epithelium. *Investig. Ophthalmol. Visual Sci.* **59**, 4028–4028 (2018).
14. Reichman, S. et al. Generation of storable retinal organoids and retinal pigmented epithelium from adherent human iPS cells in xeno-free and feeder-free conditions. *Stem Cells* **35**, 1176–1188 (2017).
15. Reichman, S. et al. From confluent human iPS cells to self-forming neural retina and retinal pigmented epithelium. *Proc. Natl Acad. Sci. USA* **111**, 8518–8523 (2014).

16. Abu Khamidakh, A. E. et al. Wound healing of human embryonic stem cell-derived retinal pigment epithelial cells is affected by maturation stage. *BioMed. Eng. OnLine* **17**, 102 (2018).
17. Barron, J., Fleet, D., Beauchemin, S. & Burkitt, T. Performance of optical flow techniques. In *Proc. 1992 IEEE Computer Society Conference on Computer Vision and Pattern Recognition*, 236–242 (IEEE, 1992).
18. Lamprecht, M. R., Sabatini, D. M. & Carpenter, A. E. CellProfiler™: free, versatile software for automated biological image analysis. *BioTechniques* **42**, 71–75 (2007).
19. Bonilha, V. L., Finnemann, S. C. & Rodriguez-Boulan, E. Ezrin promotes morphogenesis of apical microvilli and basal infoldings in retinal pigment epithelium. *J. Cell Biol.* **147**, 1533–1548 (1999).
20. Bonilha, V. L. Retinal pigment epithelium (RPE) cytoskeleton in vivo and in vitro. *Exp. Eye Res.* **126**, 38–45 (2014).
21. Atlan, M. Holovibes: hologram rendering made easy http://holovibes.com/ (2014).
22. Geiger, B., Bershadsky, A., Pankov, R. & Yamada, K. M. Transmembrane crosstalk between the extracellular matrix and the cytoskeleton. *Nat. Rev. Mol. Cell Biol.* **2**, 793–805 (2001).
23. Arnoult, D. Mitochondrial fragmentation in apoptosis. *Trends Cell Biol.* **17**, 6–12 (2007).
24. Ahmad, T. et al. Computational classification of mitochondrial shapes reflects stress and redox state. *Cell Death Dis.* **4**, e461–e461 (2013).
25. Miyazono, Y. et al. Uncoupled mitochondria quickly shorten along their long axis to form indented spheroids, instead of rings, in a fission-independent manner. *Sci. Rep.* **8**, 350 (2018).
26. Hergott, G. J., Nagai, H. & Kalnins, V. I. Inhibition of retinal pigment epithelial cell migration and proliferation with monoclonal antibodies against the beta 1 integrin subunit during wound healing in organ culture. *Investig. Ophthalmol. Visual Sci.* **34**, 2761–2768 (1993).
27. Jacinto, A., Martinez-Arias, A. & Martin, P. Mechanisms of epithelial fusion and repair. *Nat. Cell Biol.* **3**, E117–123 (2001).
28. Farooqui, R. & Fenteany, G. Multiple rows of cells behind an epithelial wound edge extend cryptic lamellipodia to collectively drive cell-sheet movement. *J. Cell Sci.* **118**, 51–63 (2005).
29. Paques, M. et al. Adaptive optics ophthalmoscopy: application to age-related macular degeneration and vascular diseases. *Prog. Retin. Eye Res.* **66**, 1–16 (2018).
30. Croze, R. H., Thi, W. J. & Clegg, D. O. ROCK inhibition promotes attachment, proliferation, and wound closure in human embryonic stem cell-derived retinal pigmented epithelium. *Transl. Vis. Sci. Technol.* **5**, 7–7 (2016).
31. Gocho, K. et al. Adaptive optics imaging of geographic atrophy. *Investig. Ophthalmol. Visual Sci.* **54**, 3673–3680 (2013).
32. Huang, D. et al. Optical coherence tomography. *Science* **254**, 1178–1181 (1991).
33. Beaurepaire, E., Boccara, A. C., Lebec, M., Blanchot, L. & Saint-Jalmes, H. Full-field optical coherence microscopy. *Opt. Lett.* **23**, 244–246 (1998).
34. Dubois, A., Vabre, L., Boccara, A.-C. & Beaurepaire, E. High-resolution full-field optical coherence tomography with a Linnik microscope. *Appl. Opt.* **41**, 805–812 (2002).
35. Dubois, A. et al. Ultrahigh-resolution full-field optical coherence tomography. *Appl. Opt.* **43**, 2874–2883 (2004).
36. Apelian, C., Harms, F., Thouvenin, O. & Boccara, C. Dynamic full field optical coherence tomography: subcellular metabolic contrast revealed in tissues by interferometric signals temporal analysis. *Biomed. Opt. Express* **7**, 1511 (2016).
37. Thouvenin, O. et al. Cell motility as contrast agent in retinal explant imaging with full-field optical coherence tomography. *Investig. Ophtalmol. Visual Sci.* **58**, 4605 (2017).
38. Fronk, A. H. & Vargis, E. Methods for culturing retinal pigment epithelial cells: a review of current protocols and future recommendations. *J. Tissue Eng.* **7**, 2041731416650838 (2016).
39. Liang, R. et al. Lycium barbarum polysaccharide protects ARPE-19 cells against H_2O_2-induced oxidative stress via the Nrf2/HO-1 pathway. *Mol. Med. Rep.* **24**, 769 (2021).
40. Muangnoi, C. et al. Protective effects of a lutein ester prodrug, lutein diglutaric acid, against H_2O_2-induced oxidative stress in human retinal pigment epithelial cells. *Int. J. Mol. Sci.* **22**, 4722 (2021).
41. Schindelin, J. et al. Fiji: an open-source platform for biological-image analysis. *Nat. Methods* **9**, 676–682 (2012).
42. Groux, K. SAVE profiler software https://zenodo.org/record/5820201 (2022).
43. Grada, A., Otero-Vinas, M., Prieto-Castrillo, F., Obagi, Z. & Falanga, V. Research techniques made simple: analysis of collective cell migration using the wound healing assay. *J. Investig. Dermatol.* **137**, e11–e16 (2017).
44. GROUX, K. et al. Supplementary movies https://zenodo.org/record/5894962 (2022).
45. Scholler, J. FFOCT control and acquisition software https://zenodo.org/record/3137246 (2019).

Acknowledgements

The authors would like to thank Valérie Forster for providing primary porcine samples. The authors thank Jules Scholler, Pedro Mecê and Olivier Thouvenin for fruitful discussions on the results. The authors thank Marie Darche and Leyna Boucherit for their help in immunohistochemistry experiments and analysis of results. The authors would like to thank the direction and management teams of the institutions involved. The authors thank the following sources of funding: OREO [ANR-19-CE19-0023], IHU FOReSIGHT [ANR-18-IAHU-0001], HELMHOLTZ (European Research Council (ERC) (#610110)), OPTORETINA (European Research Council (ERC) (#101001841)), LabEx LIFESENSES [ANR-10-LABX-0065], Institut Carnot Fondation Voir et Entendre, RETINIT-iPS [ANR-19-CE18-0005], LabEx WIFI, [ANR-10-LABX-0024].

Author contributions

K. Gro. performed the D-FFOCT experiments and wrote the wound analysis softwares. A.V. performed the immunohistochemistry experiments. S.R., C.N. and M.C. provided the hiRPE samples. K. Gri., S.R., C.B. and M.P. designed the experiments. All authors (K. Gro., A.V., S.R., C.N., M.C., K. Gri., C.B., M.P., M.F. and J.-A.S.) discussed the results. K. Gro., A.V., S.R. and K. Gri. wrote the paper.

Competing interests

The authors declare no competing interests.

Additional information

Supplementary information The online version contains supplementary material available at https://doi.org/10.1038/s42003-022-03479-6.

Correspondence and requests for materials should be addressed to Kassandra Groux or Kate Grieve.

Peer review information *Communications Biology* thanks Ireneusz Grulkowski and the other, anonymous, reviewer(s) for their contribution to the peer review of this work. Primary Handling Editors: Chao Zhou and Anam Akhtar.

Reprints and permission information is available at http://www.nature.com/reprints

Publisher's note Springer Nature remains neutral with regard to jurisdictional claims in published maps and institutional affiliations.

Open Access This article is licensed under a Creative Commons Attribution 4.0 International License, which permits use, sharing, adaptation, distribution and reproduction in any medium or format, as long as you give appropriate credit to the original author(s) and the source, provide a link to the Creative Commons license, and indicate if changes were made. The images or other third party material in this article are included in the article's Creative Commons license, unless indicated otherwise in a credit line to the material. If material is not included in the article's Creative Commons license and your intended use is not permitted by statutory regulation or exceeds the permitted use, you will need to obtain permission directly from the copyright holder. To view a copy of this license, visit http://creativecommons.org/licenses/by/4.0/.

© The Author(s) 2022